Supplementary Material for:

Engineering gallium phosphide nanostructures for efficient nonlinear photonics and enhanced spectroscopies

Gianni Q. Moretti[1], *Emiliano Cortés*[2], *Stefan A. Maier*[2,3], *Andrea V. Bragas*[1] *and Gustavo Grinblat*[1*]

[1]Departamento de Física, FCEN, IFIBA-CONICET, Universidad de Buenos Aires, C1428EGA Buenos Aires, Argentina

[2]Chair in Hybrid Nanosystems, Nanoinstitute Munich, Faculty of Physics, Ludwig-Maximilians-Universität München, 80539 München, Germany.

[3]Department of Physics, Imperial College London, London SW7 2AZ, UK

*Corresponding author. Email: grinblat@df.uba.ar

Contents

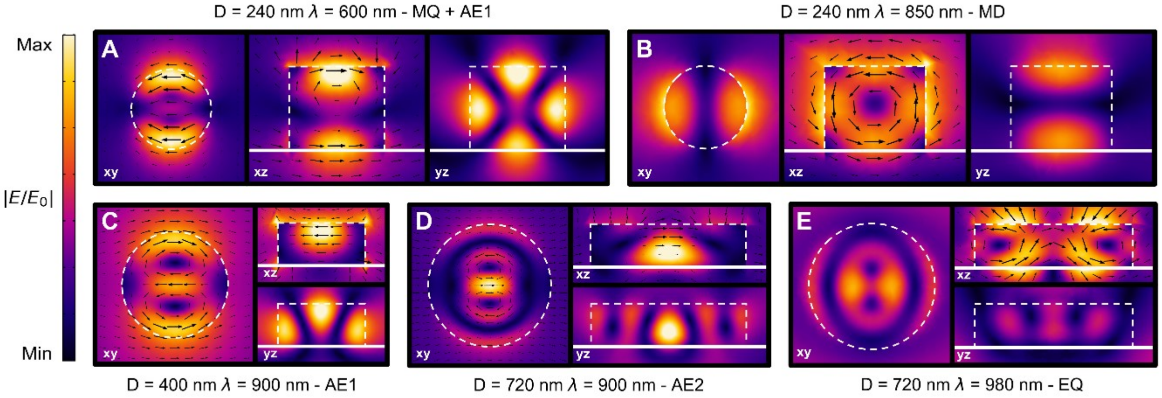

Figure S1: Electric near-field distributions for the disk nanoantennas. (A-E) Different cuts of the nanodisk for the (A) hybridized magnetic quadrupole and anapole excitation (MQ+AE1), (B) magnetic dipole (MD), (C) first-order anapole excitation (AE1), (D) second-order anapole excitation (AE2) and (E) electric quadrupole (EQ). The MD resonance in Figure 4A for D = 280 nm delivers the highest SHG efficiency among all nanoantennas, while the mixing of this mode with MQ+AE1 for D = 240 nm yields the maximum DFWM efficiency in Figure 4C.

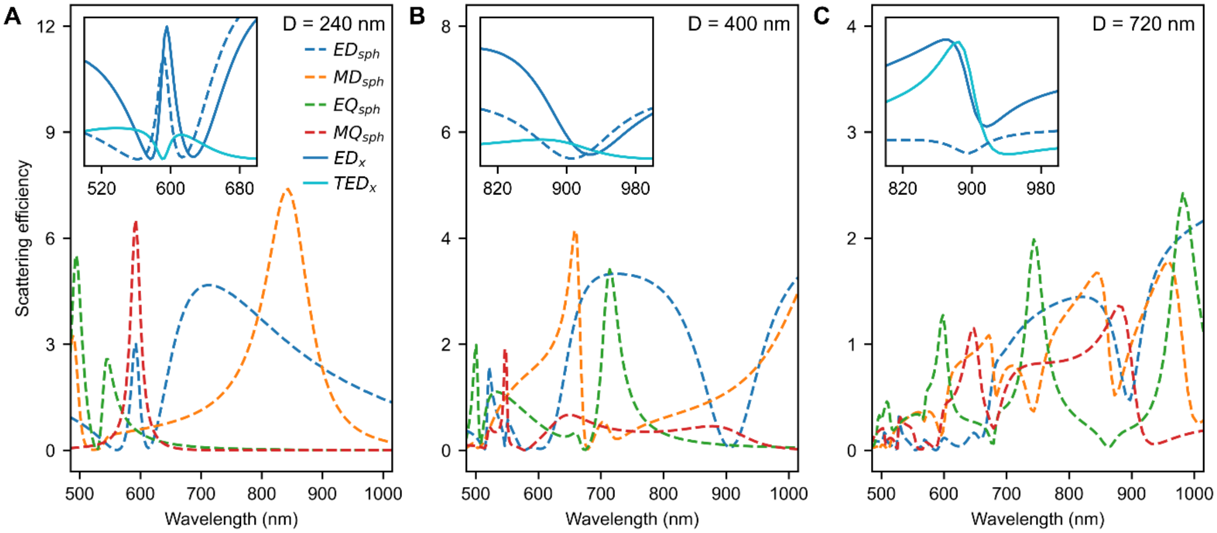

Figure S2: Multipolar decompositions for selected disk nanoantennas. (A-C) Spherical multipoles for different disk diameters describing the resonances shown in Figure S1. The insets detail the contribution of cartesian multipoles to highlight the anapole excitations, which are obtained when the cartesian electric dipole (ED) and toroidal electric dipole (TED) have the same weight, but opposite phase, canceling each other out in the far-field and giving zero scattering in the spherical ED counterpart.

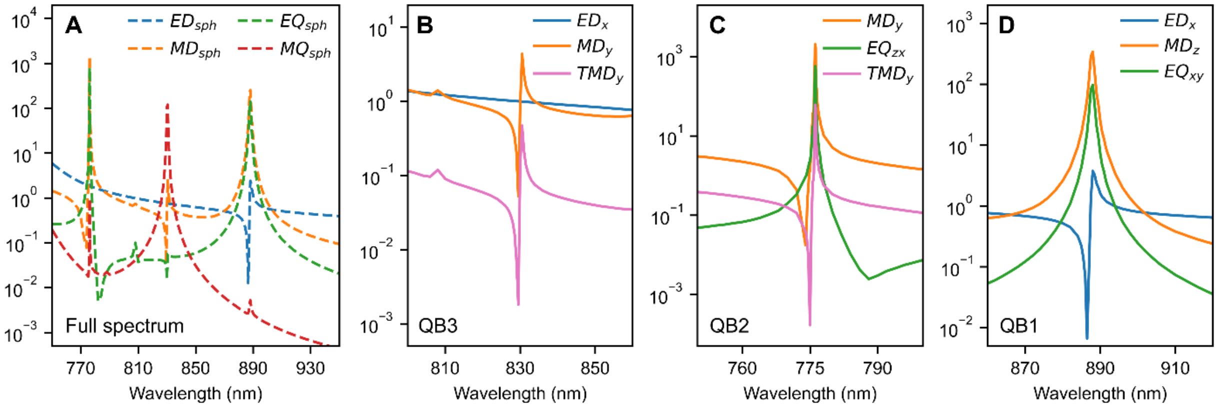

Figure S3: Multipolar decompositions of the QBIC resonances in the metasurface. (A) Multipolar decomposition in spherical harmonics of the periodic array linearly characterized in Figure 3B,C, but suspended in air (the resonant wavelengths appear therefore shifted with respect to the main text or Figure S4). **(B-D)** Detailed cartesian decomposition of the three QBICs analyzed, QB1 (D), QB2 (C), and QB3 (B). QB1 supports an out-of-plane magnetic dipole and an in-plane electric quadrupole, which can be externally excited with an x-polarized incident wave through the induced electric dipole in the horizontal direction, as enabled by the tilting of the meta-atoms. The highest contribution in QB2 comes from the in-plane magnetic dipole, which couples the two elements in the unit cell forming an electric quadrupole in the *xz* plane. A toroidal magnetic dipole also appears when deriving the irreducible forms of higher order cartesian moments. In the case of QB3, the field distribution in Figure 3C shows two electric field circulations in opposite directions, inducing magnetic dipoles that cancel each other out in the *x* direction but add in the *y* direction, because of the tilting of the elliptical disks, explaining the highest component seen in panel B here.

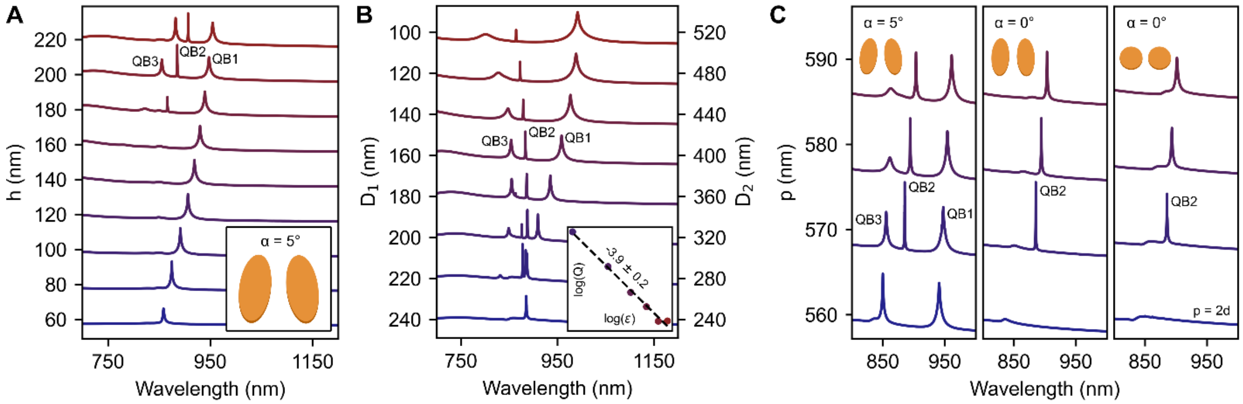

Figure S4: Geometric variations of the metasurface characterizing the different QBIC resonances. (A,B) Dependence of the average field intensity enhancement inside the dielectric ($\langle |E/E_0|^2 \rangle$) on the height (A) and shape (B) of the elliptical disks, while keeping the other dimensions as in Figure 3B. It can be seen that a minimum height is required for sustaining the three different QBICs simultaneously. For QB1, a relation between the quality factor and the eccentricity ($\varepsilon = \sqrt{1 - D_1/D_2}$) was obtained, yielding $Q \propto \varepsilon^{-3.9}$ (inset in B). When the disk cross-section changes from elliptical to circular the only resonance remaining is QB2. **(C)** Dependence of $\langle |E/E_0|^2 \rangle$ on the period of the metasurface for tilted (left graph) and parallel (middle) elliptical cylinders, and circular disks (right). The asymmetry characterizing the QB2 state is the difference between the inner-cell and inter-cell spacing of disks. In the three graphs this peak disappears when the distance between all cylinders in the metasurface is the same ($p = 2d$).

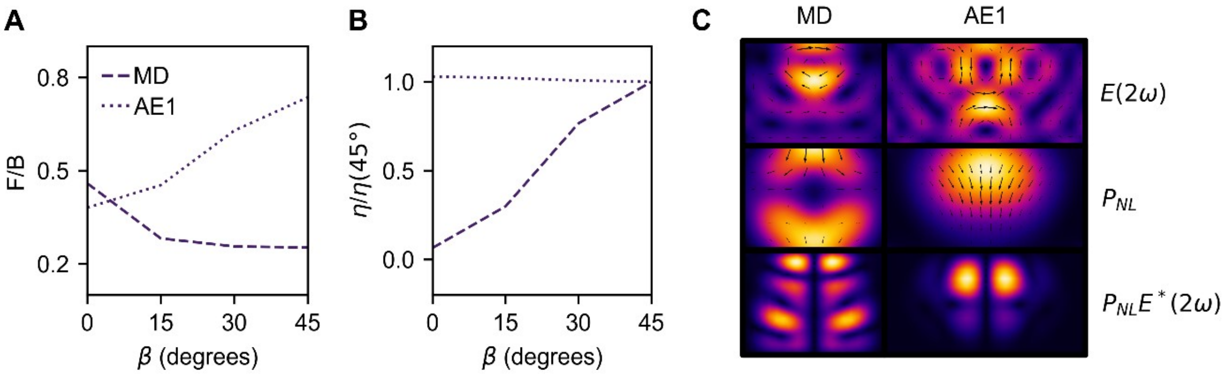

Figure S5: Additional SHG results of the nanoantennas. (A) Forward-to-backward SH power ratio when changing the in-plane crystal orientation β, when pumping at the MD or AE1 resonances. **(B)** Dependence of the SHG efficiency on β for the resonances analyzed in A. Efficiencies are normalized by their corresponding values at $\beta = 45°$. **(C)** Effect of the linear fields at the fundamental and emission frequencies on the nonlinear coupling integral Γ_{SHG}, when pumping at the MD (left) and AE1 (right). The first row is the distribution of the linear electric field inside the dielectric at the emission frequency, the second is the nonlinear polarization induced by the fundamental fields, and the third is the integrand in the equation defining Γ_{SHG} (see main text). The resulting overlap is larger when exciting at the MD mode compared to the AE1 state, and thus a higher SHG efficiency is obtained for the former in Figure 4A.

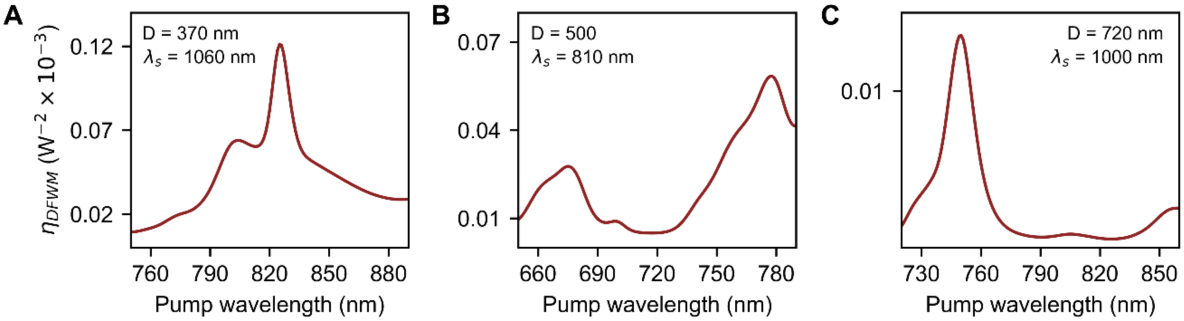

Figure S6: Other mode mixings studied in the nanoantennas. (A-C) DFWM conversion efficiencies as a function of the pump wavelength for different disk diameters. The signal wavelength is set at the MD in A, and the EQ in B and C. The maximum efficiency reported in Figure 4C is more than one order of magnitude higher than the best case presented here.

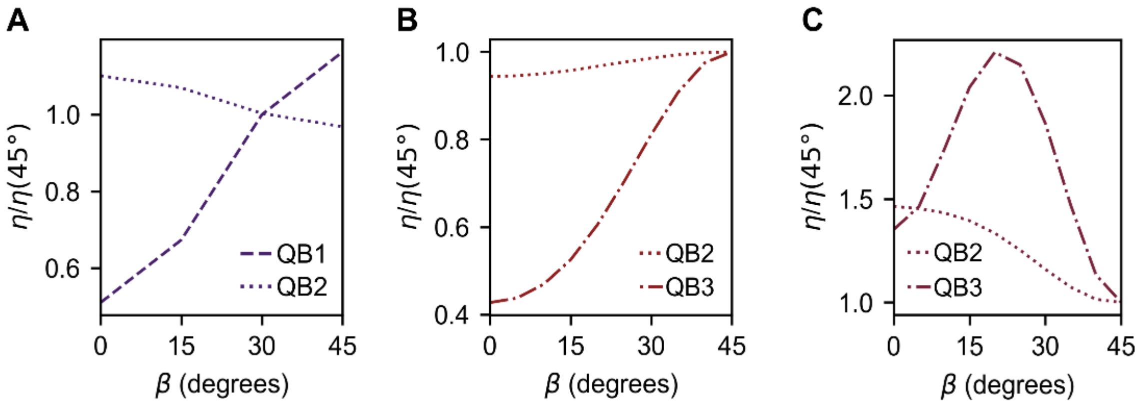

Figure S7. Second- and third-order nonlinear efficiencies of the metasurface when changing β. (A-C) Nonlinear efficiencies normalized by their corresponding values at $\beta = 45°$ for the processes described in Figure 5 A-C, respectively. They are found to vary only within a factor of ~2 in all the β range.

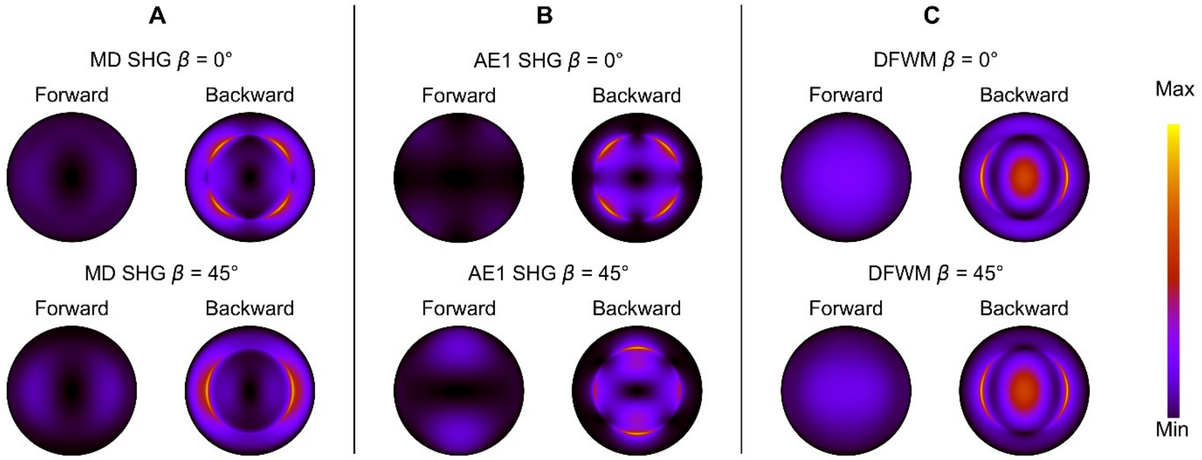

Figure S8: Forward and backward radiation patterns of the nonlinear fields in the nanoantennas. (A, B) Results for SHG when pumping at the MD (A) and AE1 (B) resonances, for $\beta = 0°$ and $45°$. **(C)** DFWM radiation distributions at the condition of maximum efficiency in Figure 4C. The nonlinear light is emitted preferentially in opposite direction to the incident waves in all cases.

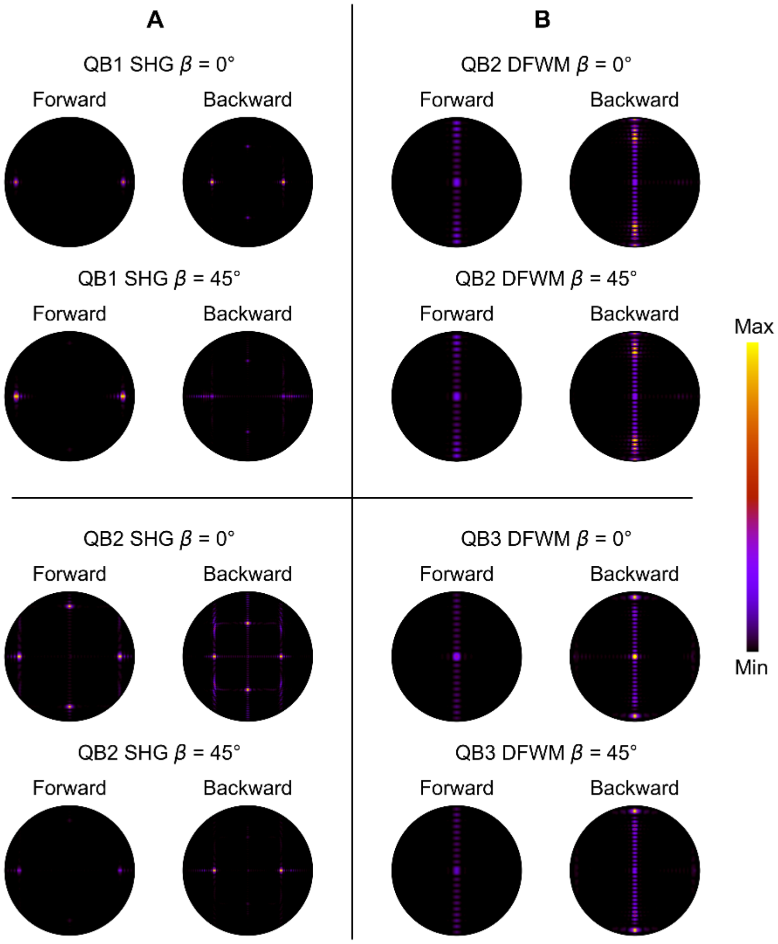

Figure S9: Forward and backward radiation patterns of selected nonlinear fields in the metasurface. **(A, B)** Nonlinear results for the most efficient SHG and DFWM processes studied in Figure 5A,B, respectively, for $\beta = 0°$ and 45°.